

An oxyl/oxo mechanism for dioxygen bond formation in PSII revealed by X-ray free electron lasers

Michihiro Suga^{1,2,†,*}, Fusamichi Akita^{1,2,†}, Keitaro Yamashita^{3,¶}, Yoshiki Nakajima¹, Go Ueno³, Hongjie Li^{1,4}, Takahiro Yamane¹, Kunio Hirata³, Yasufumi Umena¹, Shinichiro Yonekura¹, Long-Jiang Yu¹, Hironori Murakami⁵, Takashi Nomura^{3,4}, Tetsunari Kimura⁶, Minoru Kubo^{3,4}, Seiki Baba⁵, Takashi Kumasaka⁵, Kensuke Tono^{3,5}, Makina Yabashi^{3,5}, Hiroshi Isobe¹, Kizashi Yamaguchi^{7,8}, Masaki Yamamoto³, Hideo Ago^{3,*}, and Jian-Ren Shen^{1,*}

¹Research Institute for Interdisciplinary Science and Graduate School of Natural Science and Technology, Okayama University, 3-1-1 Tsushima Naka, Okayama 700-8530, Japan.

²Japan Science and Technology Agency, PRESTO, 4-1-8 Honcho, Kawaguchi, Saitama 332-0012, Japan.

³RIKEN SPring-8 Center, 1-1-1 Kouto, Sayo-cho, Sayo-gun, Hyogo 679-5148, Japan.

⁴Department of Picobiology, Graduate School of Life Science, University of Hyogo, 3-2-1 Kouto. Kamigori-cho, Ako-gun, Hyogo 678-1297, Japan.

⁵Japan Synchrotron Radiation Research Institute, 1-1-1 Kouto, Sayo, Hyogo 679-5198, Japan.

⁶Department of Chemistry, Graduate School of Science, Kobe University, 1-1 Rokkodai, Nada-ku, Kobe 657-8501, Japan.

⁷The Institute for Scientific and Industrial Research, Osaka University, Japan

⁸Institute for Nanoscience Design, Osaka University, Toyonaka, Osaka, 560-8531, Japan.

† These authors contributed equally to this work.

¶ Present address: Department of Biological Science, Graduate School of Science, The University of Tokyo, 7-3-1, Hongo, Bunkyo-ku, Tokyo, 113-0033, Japan.

*Corresponding authors.

Michihiro Suga, E-mail: michisuga@okayama-u.ac.jp

Hideo Ago, E-mail: ago@spring8.or.jp

Jian-Ren Shen, E-mail: shen@cc.okayama-u.ac.jp

Abstract

Photosynthetic water oxidation is catalyzed by the Mn₄CaO₅-cluster of photosystem II (PSII) with linear progression through five S-state intermediates (S₀-S₄). To reveal the mechanism of water oxidation, we analyzed structures of PSII in the S₁, S₂, and S₃ states by x-ray free-electron laser serial crystallography. While no insertion of water was found in S₂, flipping of D1-Glu-189 upon transition to S₃ leads to the opening of a water channel and provides a space for incorporation of an additional oxygen ligand, resulting in an open-cubane Mn₄CaO₆-cluster with an oxyl/oxo bridge. Structural changes of PSII between the different S-states reveal cooperative action of substrate water access, proton release, and O=O bond formation in photosynthetic water oxidation.

One Sentence Summary:

Intermediate S_i -state structures of PSII were analyzed by XFELs, revealing the mechanism of photosynthetic oxygen evolution.

5 **Main Text:**

Oxygenic photosynthesis by plants, algae, and cyanobacteria converts light energy from the sun into chemical energy in the form of sugar and concurrently releases dioxygen into the atmosphere, thereby sustaining all aerobic life on the Earth. The first reaction in oxygenic photosynthesis occurs in PSII, which harbors the oxygen-evolving complex (OEC) that catalyzes stepwise oxidation of water through the S-state which includes the ground state S_0 and four oxidized intermediates, S_1 - S_4 (1, 2). Dioxygen is generated in the final step of the S-state transition $S_3 \rightarrow (S_4) \rightarrow S_0$ (3). The OEC contains a Mn_4CaO_5 -cluster organized in a distorted-chair form, in which an external Mn is attached to a Mn_3CaO_4 cubane by two μ -oxo O4 and O5 atoms (4, 5). In the OEC a μ -oxo O5 has unusually long distances to its nearby Mn ions, suggesting weak binding and higher reactivity. O5 may thus serve as one of the substrates for O=O bond formation (1, 4-10). Time-resolved, pump-probe x-ray free electron laser crystallographic analysis of PSII in the S_3 state at 2.35-Å resolution showed an incorporation of an oxygen O6 into the OEC in the vicinity of O5, supporting a dioxygen formation mechanism between O5 and O6 (11). This reaction can proceed via either (i) an oxo/oxyl radical coupling (12), (ii) a nucleophilic attack reaction mechanism (13), or (iii) a peroxide intermediate mechanism (14). Due to the limited resolution of the S_3 -state structure, however, the chemical entity of the oxo-intermediates (superoxo, oxyl/oxo, peroxo and hydroxo) has not been identified, therefore the reaction mechanism was not determined unambiguously.

The OEC is located at a node of five water channels (4) (Fig. 1) involved in proton release, balancing the net charge of the OEC, and inlet of substrate water (1, 15). Dislocation of water W665 in the O4-channel upon progress of the S_i -state results in closure of the 15 Å-long, water mediated hydrogen bonding network (11, 16). We previously attributed this structural change to a proton release through the O4-channel, whereas others argued that W665 serves as the source of the O6 atom involved in O=O bond formation (17, 18). Lack of a high-resolution structure of the S_2 -state has contributed to uncertainty about the structural changes leading to or from this state. To address these issues, we fixed PSII in the S_1 , S_2 , S_3 -states, and the triply-flashed 3F-state by a cryo-trapping method with micro-crystals of PSII from a thermophilic cyanobacterium *Thermosynechococcus vulcanus*. Structures at 2.15-2.50-Å resolution using fixed target, serial femtosecond crystallography are consistent with the structures at room temperature determined previously (11, 16), but allows a more accurate determination of interatomic distances in the OEC, revealing chemical entity of the intermediate O5, O6 species and the corresponding changes in the protein-ligand environment responsible for the proton exit and water inlet during the S-state cycle.

40 **Structural determination**

Single-shot diffraction images were collected in a fixed-target data collection manner at a cryogenic temperature (5, 19), in which PSII micro-crystals were used (fig. S1, see methods). Compared to serial femtosecond crystallography (SFX) of PSII with a grease matrix as the

injection medium at room temperature (11), this method reduced the sample consumption by one order of magnitude and ensured low background images, allowing us to collect diffraction images with high hit and index rates, which yielded 2.15 Å resolution datasets for PSII in the S₁, S₂, S₃ (in dataset1, tables S1, S2). We collected datasets of a triply excited 3F-state and S₁, S₂, S₃-states (in dataset-2) at 2.35-2.50 Å-resolution independently to confirm the reproducibility of the light-induced structural changes and to examine the structural changes beyond the S₃-state.

Strong peaks in the isomorphous difference Fourier maps calculated between each state (Figs 2A to C and fig. S3) indicate successful detection of the structural changes induced by the flash illuminations. Most peaks were localized in the vicinity of OEC, in agreement with the previous observations at room temperature by the SFX method (11) (Figs. 2 to 4, fig. S3). However, structural changes in the Q_B-binding site were diminished substantially, reflecting the relaxed protein environment due to the longer delay time after flash illumination in the present study (one second in the fixed-target method vs. 10 ms in the SFX method). Pairs of positive and negative density peaks were more clearly visible in the current difference maps around the OEC owing to the high resolution achieved as well as the high isomorphism between the different S-state datasets. Changes in the interatomic distances between the four Mn atoms accompanying the S_i-state transition (table S4) reflect changes of the oxidation states of the Mn ions. Difference maps between sequential states allowed us to define the order of serial structural changes induced by S-state progression.

The S₁ and S₂ states

The Mn-Mn distances in the S₁-state in our structure (Fig. 2D and table S4) are similar to the previous results (5, 11, 16, 20), with the exception that the shortest distance (Mn1-Mn2, 2.60 Å) is slightly shorter than that of previously reported. The S₂-state may adopt either an open or a closed cubane form according to theoretical studies (21, 22). The open cubane corresponds to the structure giving rise to the S = 1/2, g=2.0 electron paramagnetic resonance (EPR) multiline signal, and the closed cubane to the S=5/2, g=4.1 signal (21, 22). The S₂-state in our structure is in the open cubane form, in agreement with the absence of the g=4.1 EPR signal in cyanobacterial PSII under normal conditions (23). Difference density analysis reveals that, upon S₁-to-S₂ transition, Mn4 is shifted toward Glu-333 and Ca is moved toward Yz (Tyr-161) slightly (Fig. 2A). There is a shift of O5 toward Mn4 and a weakening or breakage of the oxy-bridge between O5 and Mn1 in the S₂-state (fig. S4). These changes are consistent with Mn4 oxidation during the S₁-S₂ transition, giving rise to a bipyramidal five coordinated Mn1 and an open-cubane OEC structure consistent with a charge distribution of (Mn1, Mn2, Mn3, Mn4) = (III, IV, IV, IV). Slight changes in Mn-Mn distances are observed in the S₂-state (Fig. 2E), resulting in an increased homogeneity in these distances consistent with XAFS measurements (24).

In addition to the structural changes of OEC, strong negative densities were found for two water molecules W665 and W571 that are hydrogen-bonded with ligand residues of the OEC (Fig. 2A, 2C). These changes have been found in the S₁-to-S₃ transition (5), but the present results show that these two water molecules become highly disordered already in the S₁-to-S₂ transition; therefore the possibility of W665 as the substrate for O=O bond formation (17, 18) is unlikely. W665 is the second water molecule from O4 within the 15 Å long O4-water chain which ends at a water cluster consisting of five water molecules exposed to the luminal solution (Fig. 1B). This water cluster may accept a proton released from OEC as a protonated Eigen

cation through the Grotthuss-type proton transfer (25), consistent with Fourier transform infrared (FT-IR) spectroscopy that showed changes in a highly polarized hydrogen-bond network (26-28) or possible formation of a $n\text{H}_2\text{O}(\text{H}_3\text{O})^+$ cluster in the S_2 state (29, 30). Despite its long-distance to the OEC, change was observed in both electron density and its shape of the water cluster (Fig. 3B). These changes may result from positive charge accumulated during the S_1 -to- S_2 transition, possibly by the ejection of a proton from the OEC through W665. The increased mobility of W665 may be required to prevent the backflow of the proton by disconnecting the water chain (Fig. 3C), and is accompanied by a slight shift of the side chain of Glu-354_{CP43} hydrogen-bonded with W665. W571 increases its mobility also on the S_2 -to- S_3 transition (Figs. 2A, C, and 3B), likely due to the accumulated positive charges on OEC. W665 appeared in its position again in the transition of S_3 to 3F state (Supplementary text, fig. S3K), indicating regeneration of the long O4 hydrogen bond network after the S_3 -state for proton transfer in the next reaction cycle.

The oxyl/oxo species in the S_3 state

Larger difference densities were observed around the OEC upon transition S_2 -to- S_3 than those for S_1 -to- S_2 (Fig. 2A, B and fig. S3B, C). Mn1, Mn2, and Mn3 are static, but Mn4 is moved toward Ser-169 (Fig. 2B), resulting in an increase in the Mn1-Mn4 distance (Fig. 2E, F). Flipping of the side chain of Glu-189, also seen at room temperature (11), provides an open space in the vicinity of O5, enabling the insertion of O6 (Fig. 4). The improved resolution of the dataset allowed us to identify the position of O6 clearly in both $F_{\text{obs}} - F_{\text{obs}}$ and $F_{\text{obs}} - F_{\text{calc}}$ difference maps and thus determine its chemical structure unambiguously (Fig. 2B, C, H). By altering the O5-O6 distance and examining the residual densities in the $F_{\text{obs}} - F_{\text{calc}}$ difference Fourier map, we found that a distance of 1.9 Å resulted in the weakest residual densities (Fig. 2G, See methods). This distance is slightly longer than the 1.5 Å we reported previously (11), and consistent with an oxyl/oxo pair for the O5 and O6 species. Distances for superoxo (1.3 Å), peroxy (1.5 Å), and hydroxy/oxo (2.4 Å) species can be excluded based on their increased residual densities. Furthermore, a hydroxy/oxo pair cannot be accommodated into the current structure due to the limited space available, unless the interatomic distance between O5 and Mn4 were shorter by 0.3 Å. A peroxy species fits with the electron density similarly to that of the oxyl/oxo species explaining why we could not discriminate in the previous study (11); however, the oxyl/oxo species resulted in less residual electron densities in the $F_{\text{obs}} - F_{\text{calc}}$ map and evenly distributed temperature factors for O5 and O6. The interatomic distances of OEC in the S_3 -state agree well with those of the theoretically optimized structure of S_3 when the oxyl/oxo species was assumed in the open-cubane form (table S5) (31). Thus, we conclude that the O5 and O6 pair is in an oxyl/oxo form, which would be consistent with an oxyl/oxo coupling mechanism for the O=O bond formation (31).

Movement of D1-Glu189, the only monodentate carboxylate ligand to the Mn_4CaO_5 -cluster, by 0.5 Å during the S_2 -to- S_3 transition causes an elongation of the distance between its OE1 and Ca^{2+} from 3.1 Å in the S_1 -state to 3.5 Å in the S_3 -state (Fig. 4C). The Ca^{2+} ion can be considered to have a coordination number of “7.5” or pseudo-eight-coordinated in the S_1 -state, since it has seven “normal” ligands plus D1-Glu189. In the S_3 -state, the interaction between D1-Glu189 and Ca^{2+} is much weaker, but the newly inserted O6 provides an eighth ligand to Ca^{2+} with a distance of 2.6 Å (Fig. 4C), which is made possible by ability of Ca^{2+} to adopt coordination numbers from four to eight (32). The two hydrogen atoms brought by O6 are, respectively, ejected from the active site during the S_2 -to- S_3 transition, and accepted by D1-

Glu189, which forms a hydrogen bond with O6 (Fig. 4C), giving rise to the oxyl/oxo species between O6 and O5.

The mechanism for substrate water delivery

5 Flipping of the Glu-189 side chain is correlated with motions in a short loop of CP43, including Val-410_{CP43}, that restrict the size of the O1-channel (Fig. 4A, B). Paired positive and negative densities were found around Val-410_{CP43} indicating a movement of this residue toward Glu-189 by 0.5 Å in the S₃-state. This movement significantly widens the channel radius (Fig. 4A, B),
10 which may allow water molecules to come in during the S-state transition. Strong negative difference densities were found in positions overlapping with W503, W547, and W554 as well as glycerol-526 (Gol526) present in the channel, reflecting increased mobility of these molecules in response to the channel opening in the S₃-state. Two positive difference densities in the hydrogen-bonded water network indicate the insertion of new water molecules W666 and W667 into the O1 channel (Fig. 4). The O1 channel likely serves as a conduit for substrate water entry
15 into the OEC, and the residues around Val-410_{CP-43} may serve as a “valve” to control the water-inlet channel. Movements in this region coincide with incorporation of O6 into the open cubane structure of OEC during the S₂-to-S₃ transition. Thus, Glu-189 plays a pivotal role in coupling oxidation of the OEC with the opening of the water channel and delivery of the substrate into the OEC.

Conclusions

The structural changes related with the proton release, water inlet, and O=O bond formation during the S-state cycle are summarized in Fig. 4D. The displacement of W665 in the O4-channel suggests a proton transfer from the OEC upon S₁-to-S₂ transition. Considering that
25 theoretical calculations favor O5 as a hydroxide ion in S₁ and an oxide ion in the open-cubane S₂ structure (33), and that there is no proton release to the bulk solution in the S₁-to-S₂ transition, a proton is likely ejected from the O5 site and stored as a protonated Eigen cation in PSII. The structural changes observed in the O4-channel thus provide insights into the timing of proton release and an elegant way to prevent the backflow of the released proton. Insertion of O6 occurs
30 in the S₂-to-S₃ transition, providing an oxyl/oxo species in the S₃-state. Structural changes of the Glu-189 side chain serve to couple oxidation of the catalytic site with substrate water access, proton release, and O=O bond formation via the oxyl/oxo coupling mechanism. The structure and O=O bond formation mechanism revealed here should serve as an important blue print for rational design of artificial catalysts that have a capability for oxidizing water by visible light.

References

1. J. R. Shen, The Structure of Photosystem II and the Mechanism of Water Oxidation in Photosynthesis. *Annu. Rev. Plant Biol.* **66**, 23-48 (2015).
2. N. Cox, D. A. Pantazis, F. Neese, W. Lubitz, Biological water oxidation. *Acc. Chem.Res.* **46**, 1588-1596 (2013).

3. B. F. Kok, B.; McGloin, M. , Cooperation of charges in photosynthetic O₂ evolution-I. A linear four step mechanism. *Photochem Photobiol.* **11**, 457-475 (1970).
4. Y. Umena, K. Kawakami, J. R. Shen, N. Kamiya, Crystal structure of oxygen-evolving photosystem II at a resolution of 1.9 Å. *Nature* **473**, 55-60 (2011).
5. M. Suga *et al.*, Native structure of photosystem II at 1.95 angstrom resolution viewed by femtosecond X-ray pulses. *Nature* **517**, 99-103 (2015).
6. S. Yamanaka *et al.*, Possible mechanisms for the O-O bond formation in oxygen evolution reaction at the CaMn₄O₅(H₂O)₄ cluster of PSII refined to 1.9 angstrom X-ray resolution. *Chem Phys Lett* **511**, 138-145 (2011).
7. P. E. Siegbahn, Water oxidation mechanism in photosystem II, including oxidations, proton release pathways, O-O bond formation and O₂ release. *Biochim. Biophys. Acta* **1827**, 1003-1019 (2013).
8. P. E. Siegbahn, A structure-consistent mechanism for dioxygen formation in photosystem II. *Chemistry* **14**, 8290-8302 (2008).
9. N. Cox *et al.*, Electronic structure of a weakly antiferromagnetically coupled Mn(II)Mn(III) model relevant to manganese proteins: a combined EPR, 55Mn-ENDOR, and DFT study. *Inorg. Chem.* **50**, 8238-8251 (2011).
10. I. Zaharieva *et al.*, Room-Temperature Energy-Sampling K β X-ray Emission Spectroscopy of the Mn₄Ca Complex of Photosynthesis Reveals Three Manganese-Centered Oxidation Steps and Suggests a Coordination Change Prior to O₂ Formation. *Biochemistry*, (2016).
11. M. Suga *et al.*, Light-induced structural changes and the site of O=O bond formation in PSII caught by XFEL. *Nature*, **543**, 131-135 (2017).
12. X. Li, P. E. Siegbahn, Alternative mechanisms for O₂ release and O-O bond formation in the oxygen evolving complex of photosystem II. *Phys. Chem. Chem. Phys.* **17**, 12168-12174 (2015).
13. E. M. Sproviero, J. A. Gascon, J. P. McEvoy, G. W. Brudvig, V. S. Batista, Quantum mechanics/molecular mechanics study of the catalytic cycle of water splitting in photosystem II. *J. Am. Chem. Soc.* **130**, 3428-3442 (2008).
14. H. Isobe, M. Shoji, J. R. Shen, K. Yamaguchi, Chemical Equilibrium Models for the S₃ State of the Oxygen-Evolving Complex of Photosystem II. *Inorg. Chem.* **55**, 502-511 (2016).
15. H. Dau, M. Haumann, The manganese complex of photosystem II in its reaction cycle—Basic framework and possible realization at the atomic level. *Coord. Chem. Rev.* **252**, 273-295 (2008).
16. J. Kern *et al.*, Structures of the intermediates of Kok's photosynthetic water oxidation clock. *Nature* **563**, 421-425 (2018).
17. J. Wang, M. Askerka, G. W. Brudvig, V. S. Batista, Crystallographic Data Support the Carousel Mechanism of Water Supply to the Oxygen-Evolving Complex of Photosystem II. *ACS Energy Letters*, 2299-2306 (2017).
18. K. Kawashima, T. Takaoka, H. Kimura, K. Saito, H. Ishikita, O₂ evolution and recovery of the water-oxidizing enzyme. *Nat. Commun.* **9**, 1247 (2018).
19. K. Hirata *et al.*, Determination of damage-free crystal structure of an X-ray-sensitive protein using an XFEL. *Nat. Methods*, (2014).

20. A. Tanaka, Y. Fukushima, N. Kamiya, Two Different Structures of the Oxygen-Evolving Complex in the Same Polypeptide Frameworks of Photosystem II. *J. Am. Chem. Soc.* **139**, 1718-1721 (2017).
21. H. Isobe *et al.*, Theoretical illumination of water-inserted structures of the CaMn₄O₅ cluster in the S₂ and S₃ states of oxygen-evolving complex of photosystem II: full geometry optimizations by B3LYP hybrid density functional. *Dalton Trans.* **41**, 13727-13740 (2012).
22. D. A. Pantazis, W. Ames, N. Cox, W. Lubitz, F. Neese, Two interconvertible structures that explain the spectroscopic properties of the oxygen-evolving complex of photosystem II in the S₂ state. *Angew. Chem.* **51**, 9935-9940 (2012).
23. A. Boussac, H. Kuhl, S. Un, M. Rogner, A. W. Rutherford, Effect of near-infrared light on the S₂-state of the manganese complex of photosystem II from *Synechococcus elongatus*. *Biochemistry* **37**, 8995-9000 (1998).
24. C. Glockner *et al.*, Structural changes of the oxygen-evolving complex in photosystem II during the catalytic cycle. *J. Biol. Chem.* **288**, 22607-22620 (2013).
25. K. Saito, A. William Rutherford, H. Ishikita, Energetics of proton release on the first oxidation step in the water-oxidizing enzyme. *Nat. Commun.* **6**, 8488 (2015).
26. T. Noguchi, M. Sugiura, Structure of an active water molecule in the water-oxidizing complex of photosystem II as studied by FTIR spectroscopy. *Biochemistry* **39**, 10943-10949 (2000).
27. T. Noguchi, H. Suzuki, M. Tsuno, M. Sugiura, C. Kato, Time-resolved infrared detection of the proton and protein dynamics during photosynthetic oxygen evolution. *Biochemistry* **51**, 3205-3214 (2012).
28. R. J. Debus, Evidence from FTIR difference spectroscopy that D1-Asp61 influences the water reactions of the oxygen-evolving Mn₄CaO₅ cluster of photosystem II. *Biochemistry* **53**, 2941-2955 (2014).
29. J. M. Headrick *et al.*, Spectral signatures of hydrated proton vibrations in water clusters. *Science* **308**, 1765-1769 (2005).
30. B. C. Polander, B. A. Barry, Detection of an intermediary, protonated water cluster in photosynthetic oxygen evolution. *Proc. Nat. Acad. Sci. U.S.A.* **110**, 10634-10639 (2013).
31. H. Isobe, M. Shoji, T. Suzuki, J. R. Shen, K. Yamaguchi, Spin, Valence, and Structural Isomerism in the S₃ State of the Oxygen-Evolving Complex of Photosystem II as a Manifestation of Multimetallic Cooperativity. *J Chem Theory Comput*, **15**, 2375-2391 (2019).
32. I. Dokmanic, M. Sikic, S. Tomic, Metals in proteins: correlation between the metal-ion type, coordination number and the amino-acid residues involved in the coordination. *Acta Crystallogr. Sec. D, Biol. Crystallogr.* **64**, 257-263 (2008).
33. M. Shoji *et al.*, Theoretical studies of the damage-free S-1 structure of the CaMn₄O₅ cluster in oxygen-evolving complex of photosystem II. *Chem Phys Lett* **623**, 1-7 (2015).
34. A. Barty *et al.*, Cheetah: software for high-throughput reduction and analysis of serial femtosecond X-ray diffraction data. *J. Appl. Crystallogr.* **47**, 1118-1131 (2014).
35. T. A. White *et al.*, CrystFEL: a software suite for snapshot serial crystallography. *J. Appl. Crystallogr.* **45**, 335-341 (2012).
36. A. J. M. Duisenberg, Indexing in Single-Crystal Diffractometry with an Obstinate List of Reflections. *J. Appl. Crystallogr.* **25**, 92-96 (1992).

37. A. G. Leslie, The integration of macromolecular diffraction data. *Acta Crystallogr. Sec. D, Biol. Crystallogr.* **62**, 48-57 (2006).
38. W. Kabsch, Processing of X-ray snapshots from crystals in random orientations. *Acta Crystallogr. Sec. D, Biol. Crystallogr.* **70**, 2204-2216 (2014).
- 5 39. P. A. Karplus, K. Diederichs, Linking crystallographic model and data quality. *Science* **336**, 1030-1033 (2012).
40. Y. Kato *et al.*, Fourier Transform Infrared Analysis of the S-State Cycle of Water Oxidation in the Microcrystals of Photosystem II. *J Phys Chem Lett*, **9**, 2121-2126 (2018).
- 10 41. N. Collaborative Computational Project, The CCP4 suite: programs for protein crystallography. *Acta Crystallogr. Sec. D, Biol. Crystallogr.* **50**, 760-763 (1994).
42. P. D. Adams *et al.*, PHENIX: a comprehensive Python-based system for macromolecular structure solution. *Acta Crystallogr. Sec. D, Biol. Crystallogr.* **66**, 213-221 (2010).
- 15 43. P. Emsley, K. Cowtan, Coot: model-building tools for molecular graphics. *Acta Crystallogr. Sec. D, Biol. Crystallogr.* **60**, 2126-2132 (2004).
44. M. Haumann *et al.*, Photosynthetic O₂ formation tracked by time-resolved x-ray experiments. *Science* **310**, 1019-1021 (2005).

20 **Acknowledgments:** The XFEL experiments were performed at SACLA with the approval of the Japan Synchrotron Radiation Research Institute (JASRI) (proposal no. 2016A8051, 2016B8070, 2017A8040, 2017B8015, 2017B8028, 2018A8009, 2018A8010) and we thank the staff at SACLA for their help. The best condition for diffraction data collection was determined at beamlines 41XU and 44XU in SPring-8 (proposal no. 2016A2542, 2016A6621, 2016B2542, 2016B6621, 2017A2535, 2017A6724, 2017B2535, 2017B6724, 2018A2530, 2018A6822, 25 2018B2530 and 2018B6822). This research was supported by the Platform Project for Supporting Drug Discovery and Life Science Research (Basis for Supporting Innovative Drug Discovery and Life Science Research (BINDS)) from AMED under Grant no JP18am0101070.

30 **Funding:** This research was supported by KAKENHI grant nos. JP16H06162, JP16H06296, JP17H05884 (M.S.), JP17H06434 (J.-R.S.) and JP16K21181 (F.A.). Support was also provided by JST, PREST grant nos. JPMJPR18G8 (M.S.) and JPMJPR16P1 (F.A.), and RIKEN Pioneering Project “Dynamic Structural Biology” to M.K. and Mas.Y.; **Author contributions:** J.-R.S., M.S., Mas.Y. and H.A. conceived the project; G.U., H.M., S.B., Ta.K., H.A., and Mas.Y developed the data collection setup; M.K., Te.K. and T.N. set up a laser system for the sample preparation; K.T. and Mak.Y. contributed to beamline operation; F.A. and Y.N. prepared the samples and grew the crystals; M.S., H.L., T.Y., Y.U., S.Y., L-J.Y., and J.-R.S. collected the diffraction data; Ke.Y., H.L., T.Y., and M.S. processed the diffraction data; M.S. determined the structure; H.I., and Ki.Y. discussed with the atomic coordinates. M.S. and J.-R.S. wrote the manuscript; and all authors contributed to the discussion and improvement of the manuscript.

40 **Competing interests:** Authors declare no competing interests. **Data and materials availability:** The atomic coordinates and structure factors have been deposited in the Protein Data Bank under the following accession codes: 6JLJ for S₁ (dataset1), 6JLK for S₂ (dataset1), 6JLL for the S₃ (dataset1), 6JLM for S₁ (dataset2), 6JLN for S₂ (dataset2), 6JLO for S₃ (dataset2), and 6JLP for the 3F. All other data used in this study are presented in the main text or supplementary materials.

Supplementary Materials:

Materials and Methods

Supplementary Text

Figs. S1-S4

5 Tables S1-S6

References (34-44)

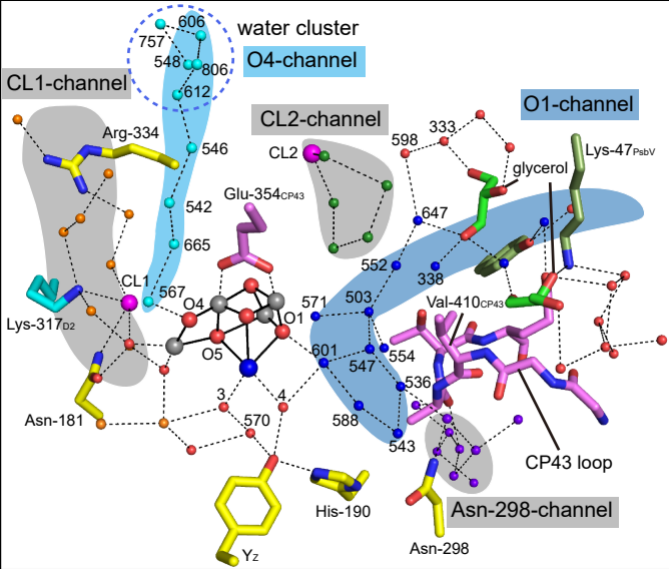
Figure legends

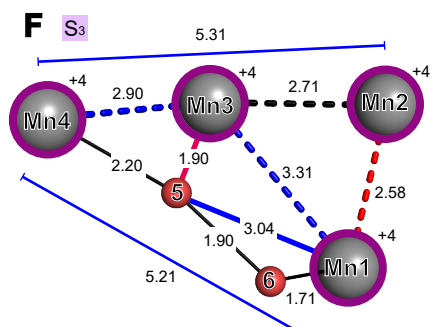
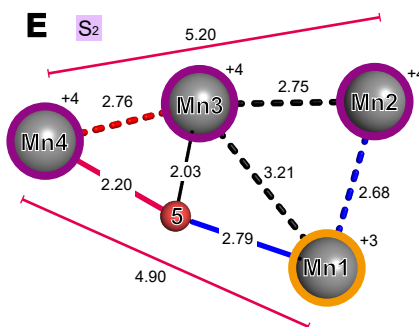
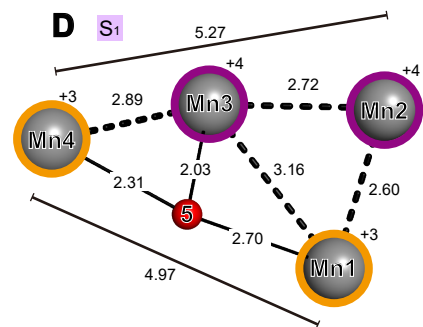
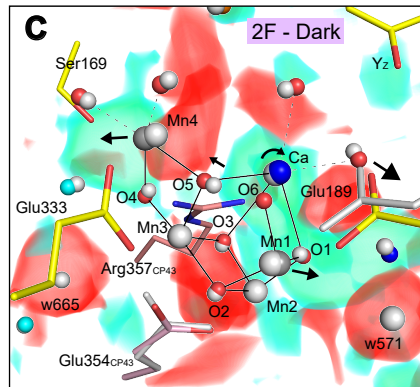
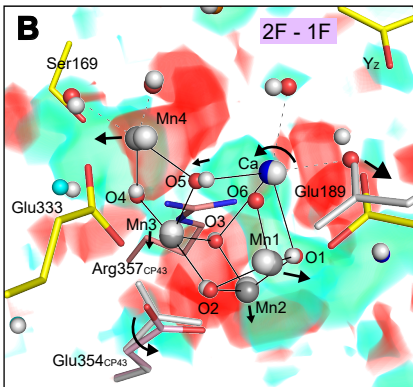
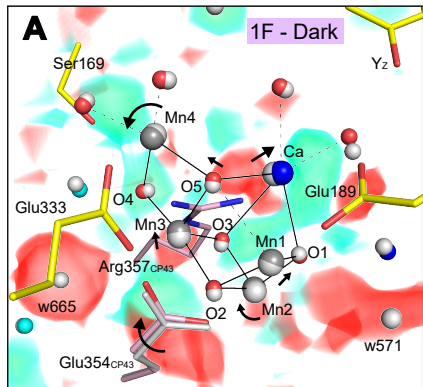
10 **Fig. 1. Water networks in PSII.** Five hydrogen-bonded water networks surround the OEC are depicted (PDB code: 4UB6). The criterion for hydrogen bond is 3.3 Å.

15 **Fig. 2. Structural changes of the OEC during the S_i -state transitions.** (A-C) OEC structures superimposed with $F_{\text{obs}} - F_{\text{obs}}$ isomorphous difference *Fourier* maps of 1F minus dark (A), 2F minus 1F (B), and 2F minus dark (C) datasets. The structures before and after the S_i -state transition are shown in gray and multi-colors, respectively, and the difference maps are contoured at -3σ (red), and 3σ (cyan), respectively. Structural changes consistent with isomorphous difference *Fourier* maps are represented by black arrows, where larger arrowheads represent the larger structural changes. (D-E) Interatomic distances (Å) of the OECs in the S_1 (D), S_2 (E) and S_3 (F) states. Blue and red lines indicate elongation and shortening of the interatomic distances compared to the structure in the precedent S_i -state. Presumed Mn (+4) and Mn (+3) cations are shown. (G) The $F_{\text{obs}} - F_{\text{calc}}$ difference *Fourier* maps contoured at -2.2σ (red) and $+2.2\sigma$ (cyan) after structural refinement by fixing the distance between O5 and O6 at 1.3 Å (superoxide), 1.5 Å (peroxo), 1.7 Å, 1.9 Å (oxyl/oxo), and 2.4 Å (hydroxo/oxo), respectively. Values in parentheses are temperature factors (Å²) of O5 and O6. Black arrows indicate the residual electron densities that were affected by the interatomic distances between O5 and O6. (H) The $F_{\text{obs}} - F_{\text{calc}}$ difference *Fourier* maps contoured at 5σ (blue) when both O5 and O6, or O6 were omitted. The color codes shown here is used for all figures unless otherwise noted.

20 **Fig. 3. Structural changes in the O4-channel.** (A) $F_{\text{obs}} - F_{\text{obs}}$ isomorphous difference *Fourier* map of 1F minus dark contoured at 3σ superimposed with the hydrogen bonding network in the O4-channel. Dislodged water molecules are highlighted by blue circles. (B) $F_{\text{obs}} - F_{\text{calc}}$ water/O6 omit (top) or $F_{\text{obs}} - F_{\text{obs}}$ (bottom) difference density values at water sites in O4-channel. (C) Possible proton transfer mechanism in the O4 channel. Hydrogen bonding network of pre (Left) and post (Right) proton transfer are shown. The proton possibly stored at the water cluster is depicted in green and indicated by a red arrow.

25 **Fig. 4. Structural changes in the water-inlet O1-channel and around the Ca^{2+} ion.** (A) Isomorphous difference map (3σ) superimposed with the O1-channel. Two water molecules that appear in S_3 state are circled in red. (B) Model of structural changes in the O1-channel. (C) The ligand environment of Ca^{2+} in the S_1 state and S_3 state. Weak interactions between Glu-189 and Ca^{2+} , and between Glu-189 and O6 are shown as blue dotted lines. Possible hydrogen atom transferred from O6 to Glu-189 is shown as a solid green line. (D) Schematic structures of OEC and the states of the O1 and O4 channels during the S_i -state. The water molecule from the O1 channel will be incorporated into O6 in the S_3 or refill the water molecules waiting for the next catalytic reaction.



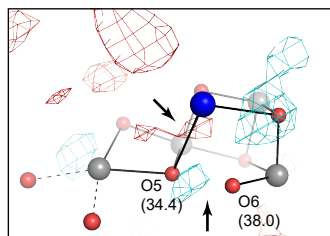
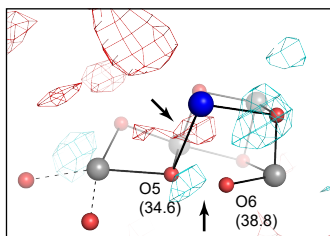
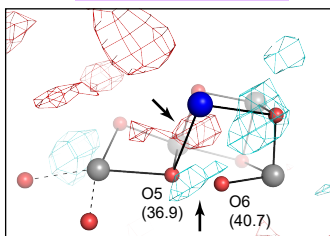
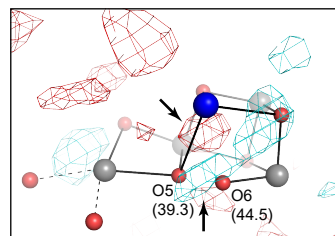


G O5-O6: 1.3 Å, superoxo

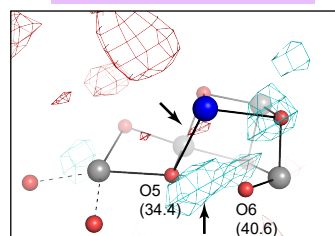
O5-O6: 1.5 Å, peroxo

O5-O6: 1.7 Å

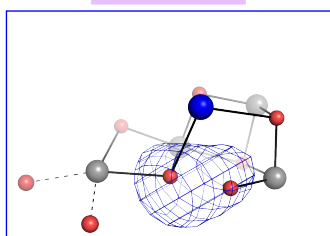
O5-O6: 1.9 Å, oxyl/oxo



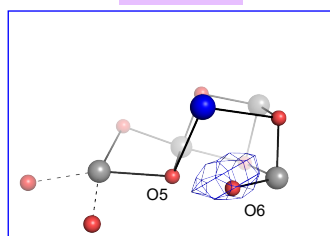
O5-O6: 2.4 Å, hydroxo/oxo

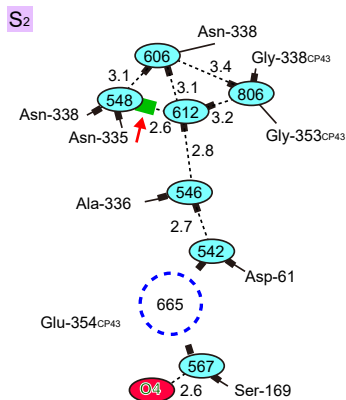
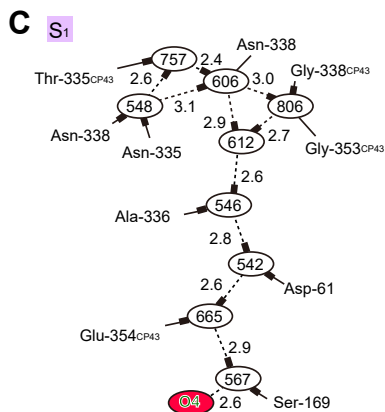
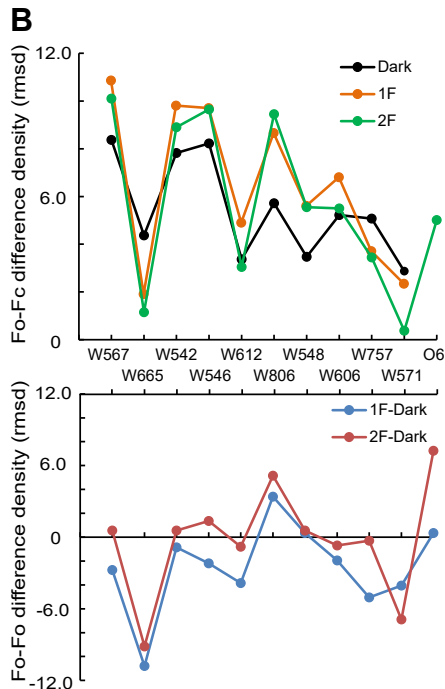
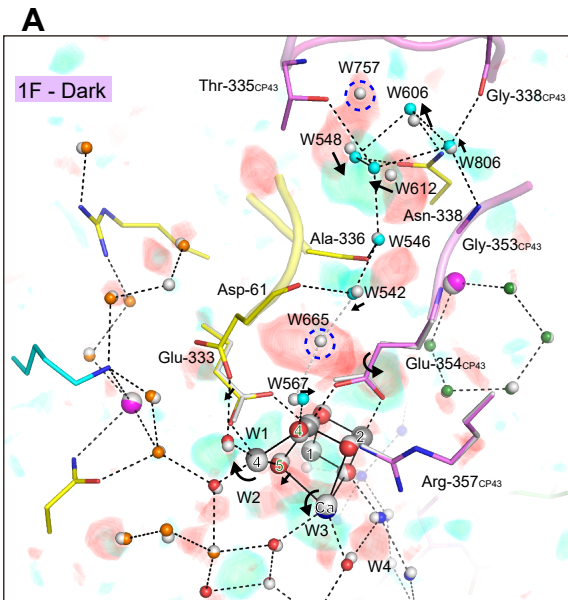


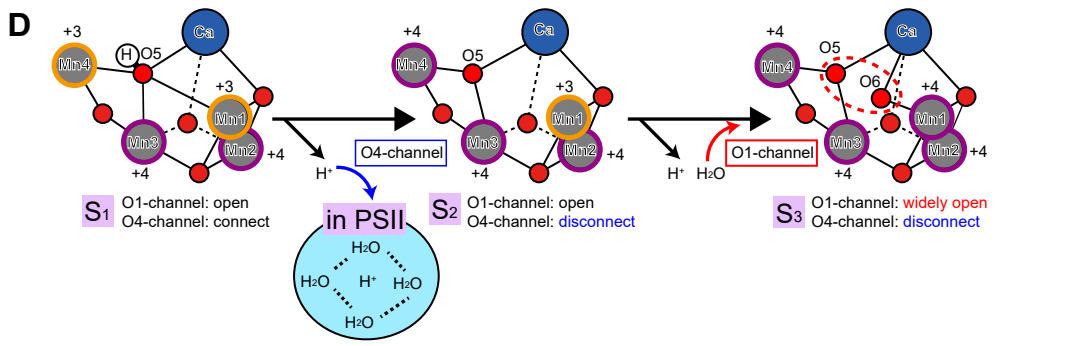
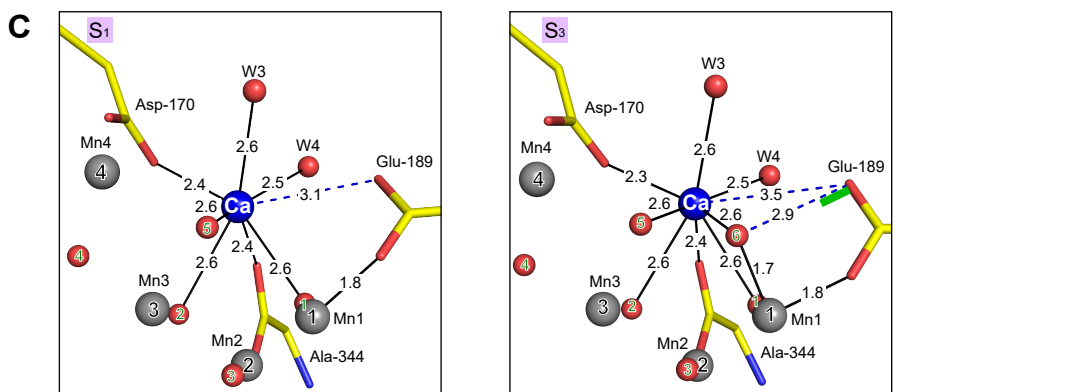
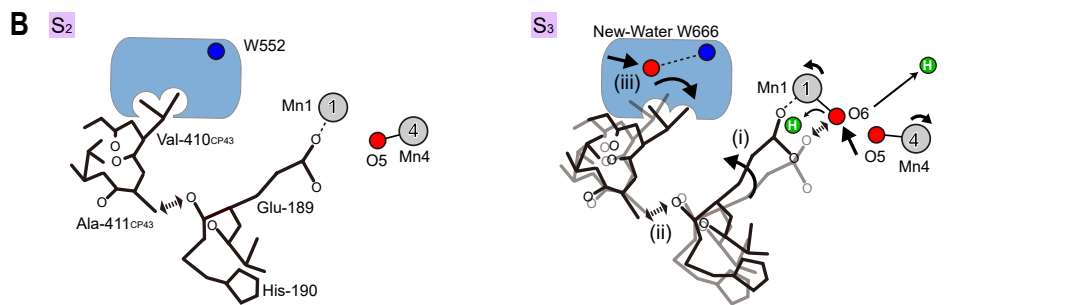
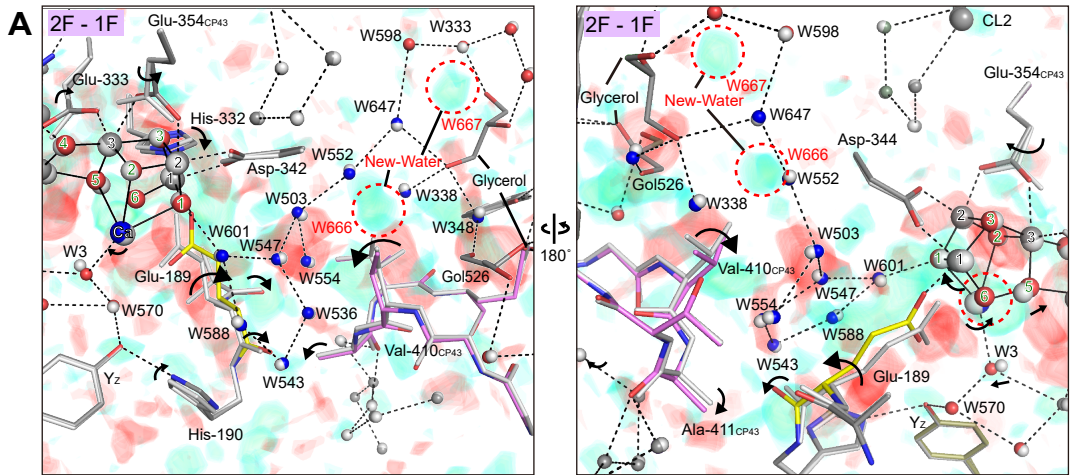
H O5-O6 omitted



O6 omitted







Supplementary Materials for
An oxy/oxo mechanism for dioxygen bond formation in PSII
revealed by X-ray free electron lasers

Michihiro Suga^{1,2,†,*}, Fusamichi Akita^{1,2,†}, Keitaro Yamashita^{3,¶}, Yoshiki Nakajima¹, Go Ueno³, Hongjie Li^{1,4}, Takahiro Yamane¹, Kunio Hirata³, Yasufumi Umena¹, Shinichiro Yonekura¹, Long-Jiang Yu¹, Hironori Murakami⁵, Takashi Nomura^{3,4}, Tetsunari Kimura⁶, Minoru Kubo^{3,4}, Seiki Baba⁵, Takashi Kumasaka⁵, Kensuke Tono^{3,5}, Makina Yabashi^{3,5}, Hiroshi Isobe¹, Kizashi Yamaguchi^{7,8}, Masaki Yamamoto³, Hideo Ago^{3,*}, and Jian-Ren Shen^{1,*}

*Corresponding authors.

Michihiro Suga, E-mail: michisuga@okayama-u.ac.jp

Hideo Ago, E-mail: ago@spring8.or.jp

Jian-Ren Shen, E-mail: shen@cc.okayama-u.ac.jp

This PDF file includes:

Materials and Methods
Supplementary Text
Figures S1-S4
Tables S1-S6
References (34-44)

Materials and Methods

Purification of Photosystem II crystals

All of the procedures for the purification, crystallization, pre-flash illumination and preparation of PSII crystals in the intermediate states were conducted in the dark or under dim green light. Highly active PSII was purified from *Thermosynechococcus vulcanus* cells and crystallized as described previously (4, 11). The crystals with an average size of 100 μm were illuminated with two pre-flashes to oxidize the tyrosine D residue (D2-Tyr160) and to decrease the possible contamination of the S_0 state. The pre-flash was provided by a Nd:YAG laser at 532 nm with a diameter of 7 mm at an energy of around 52 mJ cm^{-2} as reported previously (1). Then the crystals were dehydrated with a buffer containing 20% glycerol, 10% PEG 1,450, 10% PEG 5,000 MME, 2% dimethyl sulfoxide and 10-20 mM potassium ferricyanide by stepwise replacement of the crystallization solution over two hours. The crystals were evenly loaded onto a square mesh (1 mm x 4 mm) in which, areas of 140 μm x 140 μm were carved (fig. S1). After loading of the crystals, the extra buffer solution on the mesh was absorbed by a soft paper from the opposite side. The mesh was then illuminated with a designated number of nanosecond laser flashes at 532 nm covering the whole mesh size (with a diameter of 5.5 mm at an energy of 84 mJ cm^{-2}) and immediately frozen by a nitrogen stream (fig. S1). The interval between each flash was set to one second, which was long enough to advance the S_i -states whereas sufficiently short to prevent the decay of the intermediate S-states. By this approach, ‘light contamination’ that may occur in serial femtosecond X-ray crystallography with samples continuously ejected from a jet stream is avoided, since all the samples on the mesh are illuminated with the designated laser flashes simultaneously.

X-ray diffraction experiment and data processing

The diffraction images were collected on a Rayonix MX225HS detector with the same procedure as described for the previous SF-ROX experiments (5, 19) with slight modifications. Briefly, the mesh loaded with the PSII micro-crystals was irradiated with a single shot of XFEL pulse, and then moved by 50 μm followed by irradiation by a second XFEL pulse. This was repeated for the whole area of the mesh, which was changed to a new mesh after completion of the XFEL irradiation throughout the whole area of the mesh. The distance of 50 μm has been shown to be enough to avoid the effect of the adjacent irradiations, and therefore ensured that every diffraction image was radiation damage-free (5, 19) (fig. S1). The parameters of XFEL pulses used were as follows: pulse duration, 2-10 fs; photon flux, 9.3×10^{10} photons; pulse frequency, 10 Hz; photon energy, 10.00 keV; photon energy band width, 0.4%; beam size at the sample position, 4.8 (H) \times 4.0 (V) μm^2 .

Since the PSII micro-crystals were oriented randomly on the mesh and were not rotated during the data collection, the diffraction images obtained were processed in a way similar to that in the case of the previous SFX experiment (11). Namely, diffraction images were filtered by the program Cheetah (34) and processed by the program *CrystFEL* (35) using the known unit cell parameters and crystal symmetry of PSII. The parameters min-snr, thresholds and min-gradient used for the spot finding in *CrystFEL* were optimized and determined to be 18, 50, and 50 (dataset1), and 5, 100, 1000 (dataset2), respectively. The images were indexed using DirAx (36) and Mosflm (37) with peak integration parameters int-radius = (3, 5, 7) for dataset-1 and (4, 5, 7) for dataset-2. The Lorentz correction factor for still snapshots ($\sin(2\theta)$) were applied manually to the averaged intensities (38). The numbers of total images collected, hit images filtered by

Cheetah, indexed images, number of images used for refinement as well as the statistics for the data collection were given in table S1.

Data collection with the frozen crystals also improved the resolution, which yielded 2.15 Å resolution datasets for PSII in the S₁, S₂, S₃ (in dataset1) with high redundancy and reasonably high CC1/2 values (tables S1, S2). We further collected datasets and analyzed the structures of a triply excited 3F-state as well as S₁, S₂, S₃-states (in dataset-2) at 2.35 - 2.50 Å resolutions independently to confirm the reproducibility of the light-induced structural changes and to examine the structural changes beyond the S₃-state. We note that the intermediate structures of PSII were recently reported by SFX at room temperature at resolutions of 2.04 - 2.08 Å analyzed with datasets with CC1/2 values of 0.008 to 0.021 at the highest resolution shells and R_{iso} of 0.126 to 0.131 between the datasets (16). If we adopt the similar criterion, our data extends to 1.9 Å resolution (fig. S2). However, we found that the quality of the electron density maps was not improved by incorporating the weak reflections with the low CC1/2 values. Thus, we adopted the paired refinement strategy to determine the resolution limits in this study (39), which gave rise to 2.15 Å resolution datasets with CC1/2 values of 0.23-0.38 in the highest resolution shell and R_{iso} values of 0.073-0.081 between the different datasets (fig. S2, table S1 to S3). Therefore, the structures of the present study have accuracy similar to the ones by Kern et al. (16). The low R_{iso} values indicate a high isomorphism between the datasets, which was found to be critical to detect the meaningful small structural changes based on the isomorphous difference Fourier maps, and we will not discuss small structural changes when R_{iso} is over 0.1 (fig. S3D).

Structural refinement

The population of S_i-state in the PSII crystals after flash illuminations are based on the estimated efficiencies by ATR-FTIR measurements as reported previously (11, 40). The 1F dataset and 2F dataset were analyzed as a mixture of 40% of S₁ and 60% of S₂ for the former, and as a mixture of 49% of S₂ and 51% of S₃ for the latter, respectively. The 3F dataset was refined with the structure of 2F dataset because notable structural changes were not detected with an exception of W665. The statistics for the refinement were given in table S1.

We applied the geometry restraints as follows: No restraints were applied between Mn cations in the S₁, S₂, and S₃ structures. For the Mn-O and Ca-O interatomic distances in the S₁ structure, the average distance of the high-resolution S1 structure with loose restraints (0.06 Å, three times larger than the standard refinement error range) was applied. For the Mn-O and Ca-O interatomic distances in the S₂ structure, the same treatment was used as for the S1 structure except that the Mn-O5 distance was fixed to 2.2 Å with a tighter restraint of 0.01 Å. For the Mn-O and Ca-O interatomic distances in the S3 structure, the same treatment was used as for the S₂ structure with tight restraints (0.02 Å, same as the standard refinement error range). For the oxyl/oxo structure, an additional restraint of 1.9 Å was applied for the O5-O6 distance, and a restraint of 1.7 Å was applied for the O6-Mn1 distance, respectively, both with tight restraints of 0.02 Å.

The initial phases were obtained by molecular replacement with the program Phaser in the CCP4 suite (41) using the 1.95 Å XFEL structure of PSII (PDB code 4UB6) (11). Structural refinement was performed with Phenix (42) and the model was manually modified with COOT (43). Interatomic distances in the OEC were refined using the loose geometric restraints to the Mn-O and Ca-O bond distances, and no geometric restraints were applied between the Mn cations, which allowed us to confirm most M-O bonds found in the high-resolution structures in the S₁ state (5, 20) and detect meaningful structural changes of the OEC during the S_i-state

transitions.

For the structural refinement of the 1F data at 2.15 Å resolution, the occupancies of the S₁ structure and S₂ structures were set to 0.4 and 0.6, respectively, as described above. The region in which the structure was refined in multiple states was selected for the areas where strong difference peaks were observed in the isomorphous difference Fourier map between F_{obs} (1F) and F_{obs} (dark) as summarized in fig. S3, and the rest regions were refined as a single conformation. The S₂ state structure where changes occurred during the progress of the Kok-cycle was first refined for the coordinates but not the temperature factors, and the resultant coordinates were manually modified so that the residual electron densities in the $mF_{\text{o}}-DF_{\text{c}}$ map were minimized. The bond distance between O5 and Mn4 ion was determined by inspecting the residual electron densities in each $mF_{\text{o}}-DF_{\text{c}}$ map after the structural refinement with constraints of the corresponding bond length to 1.9, 2.0, 2.1, 2.2, 2.3, and 2.4 Å. The residual densities with the constraint of 2.2 Å was found to be the least, although those for constraints of distances to 2.3 Å and 2.4 Å were more or less similar to that of 2.2 Å (fig.S4). In contrast, the residual densities around the O5 were rapidly increased with the constraints of distances shorter than 2.2 Å. The soundness of the bond distances was also confirmed by a similar behavior in the temperature factor of O5 in multiple states; for example, the temperature factor of O5 with occupancies of 0.4 and 0.6 in the A monomer were 34.6 and 34.5, respectively with the constraint of distance to 2.2 Å, while the corresponding values were 29.0 and 39.3 with the constraint of distance to 1.9 Å, indicating that a 2.2 Å distance is appropriate for the Mn4-O5 distance. Finally, the temperature factor and TLS parameter were refined against the fixed coordinates. Similar distributions of the temperature factors were obtained for the regions refined as multiple states, suggesting that the occupancies for the S₁ and S₂ structures we used were reasonable. The refined structure obtained is in well agreement with the structural changes found in the isomorphous difference Fourier map between F_{obs} (1F) and F_{obs} (dark).

For the structural refinement of 2F data at 2.15 Å resolution, we assumed that the population of the S₁ state structure was negligible and the occupancies of the S₂ structure and S₃ structure are almost equal and are assigned as 0.49 and 0.51, respectively, based on the results of FTIR. The regions refined as multiple states were selected based on the difference map between F_{obs} (2F) and F_{obs} (1F). The strategy for the structural refinement of these regions were the same as that used for the S₂ state structure with small exceptions for the OEC. The OEC structure was refined under the bond constraints of lengths to 1.3, 1.5, 1.9 and 2.4 Å between O5 and O6, corresponding to superoxide, peroxide, oxyl-oxo, and hydroxo species, respectively. In addition, a bond distance of 1.7 Å as an intermediate distance between peroxy and oxyl-oxo was also tested. The result showed that the bond distance constrained to 1.9 Å gave rise to the least residual electron densities in the $mF_{\text{o}}-DF_{\text{c}}$ map and reasonable temperature factors of O5 and O6 that are compatible with each other as well as with their surrounding atoms (Fig. 2).

Other four datasets (dark, 1F, 2F, and 3F) were processed at 2.35 - 2.5 Å resolutions, and were refined with the coordinates in the equivalent *Si*-state refined at 2.15 Å resolutions as described above. After a few cycles of rigid body refinement, the coordinates, temperature factors, and TLS parameters of all atoms except the region refined as multiple conformations were first refined. Then all the coordinate including the multiple conformations were refined. The 3F structure was refined with the 2F structure, as these two structures were almost identical except for the site of W665.

Supplementary Text

Regeneration of the long O4 hydrogen bond network in the 3F state

The PSII microcrystals used in this study had a lowered efficiency of S-state transition beyond the S_3 -state due to the presence of a high concentration of PEG (40). Nevertheless, we collected a dataset from three-flashes illuminated (3F) state and calculated 3F minus 2F isomorphous difference *Fourier* map to examine possible structural changes prior to the onset of the O=O formation. The only difference feature found was some positive difference densities contoured at 3.5σ on W665 analyzed at 2.5 Å resolution, which reveals that W665 returns to its original position and becomes ordered (fig. S3K). This indicates that the long O4 hydrogen bond network is regenerated beyond the S_3 -state for proton transfer in the next cycle, in agreement with that reported by Kern et al. (16). No apparent structural change was found in the O1 channel, indicating that the O1 channel remains open in the 3F-illuminated structure. Therefore, we speculate that the proton release through the O4-channel precedes the oxygen evolution as well as narrowing of the O1 channel in the transition of $S_3 \rightarrow (S_4) \rightarrow S_0$. An additional S_3' state with half-time of about 200 μ s revealed by time-resolved X-ray absorption spectroscopy (XAS) (44) has been taken as evidence for proton release into the bulk solvent upon transition from S_3Y_Z to S_0Y_Z . Structural changes induced by the 3F-illumination may be relevant to this S_3' state.

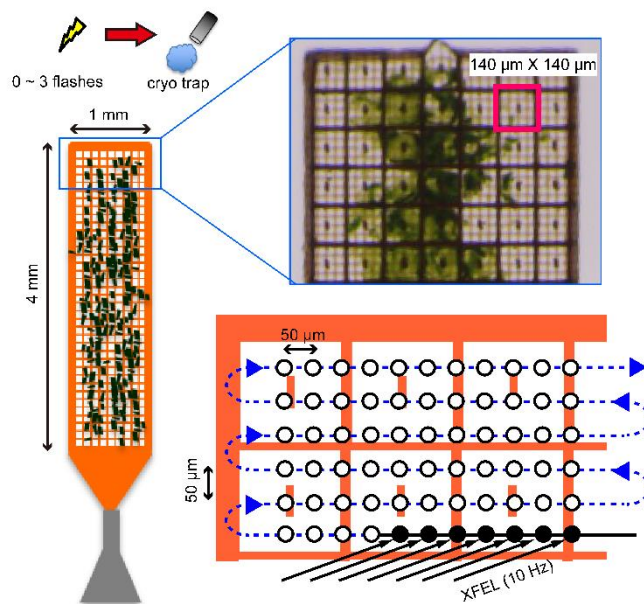


Fig. S1. Fixed-target serial femtosecond rotational crystallography (SF-ROX) of PSII.

Micro-sized crystals of PSII were sprayed on a square mesh within which, areas of $140\ \mu\text{m} \times 140\ \mu\text{m}$ were carved. The whole mesh was illuminated with a designated number of laser flashes (5 mm diameter), and then immediately flash frozen by a nitrogen stream. XFEL pulses were provided on the mesh to collect snapshots of cryo-trapped intermediate PSII at 100 K. Each irradiation spot was separated by $50\ \mu\text{m}$ to avoid influences from the adjacent irradiation.

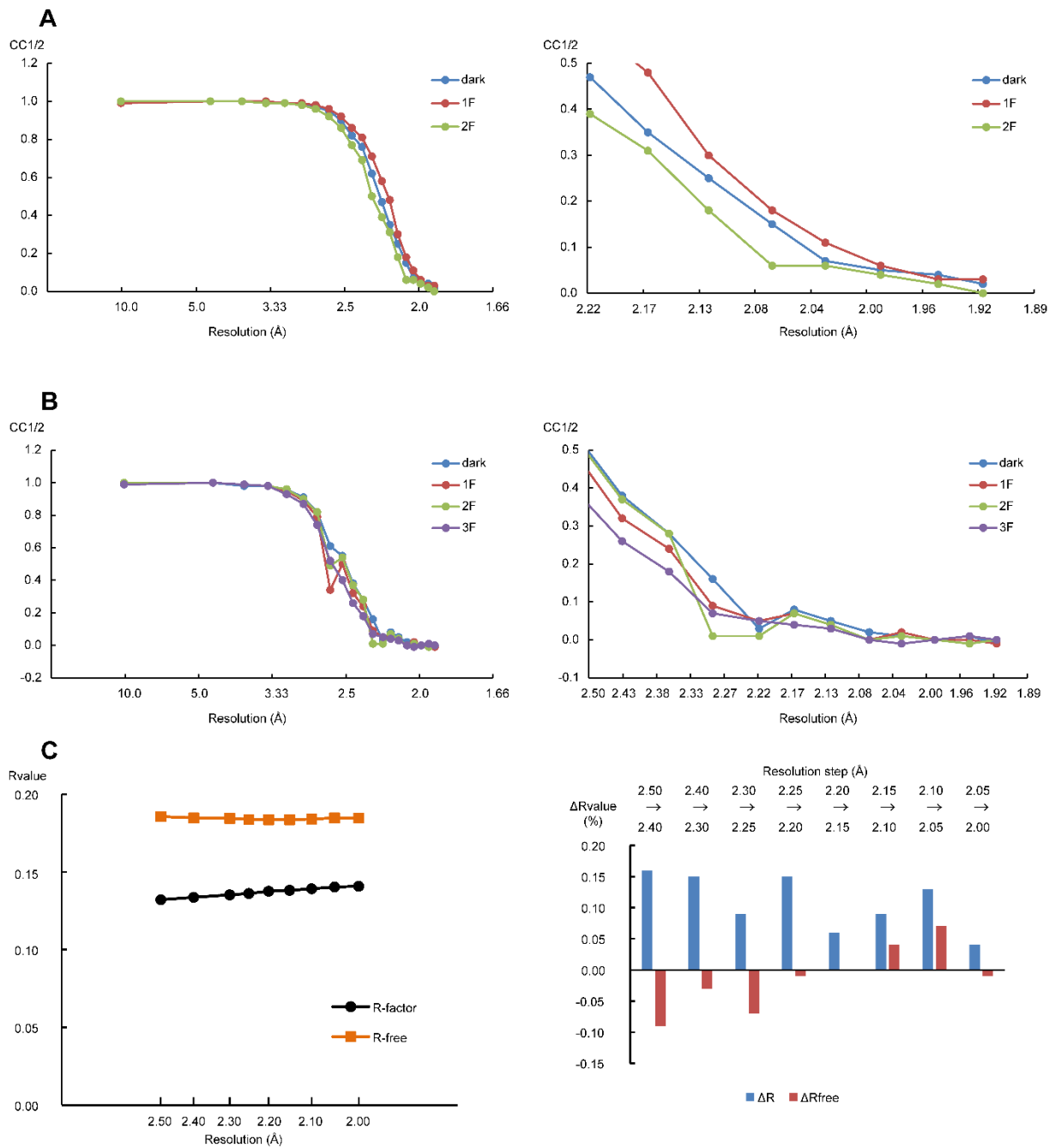


Fig. S2. Plots of CC_{1/2} vs resolution and paired refinement to evaluate the quality of data.

The plots of CC_{1/2} vs resolution were shown for the dark, 1F, and 2F datasets of dataset1 (**A**) and for dark, 1F, 2F and 3F datasets of dataset2 (**B**). In both datasets, the left panel is a plot for overall resolution, and the right panel is enlarged at around 2.0 Å resolution. (**C**) A plot of *R*- and *R*-free factors calculated up to 2.5 Å resolution when the refinement resolution limit was extended from 2.5 Å to 2.0 Å (dark, dataset-1) (left), and the differences of *R*- and *R*-free factors for each incremental step of resolution (right) were shown.

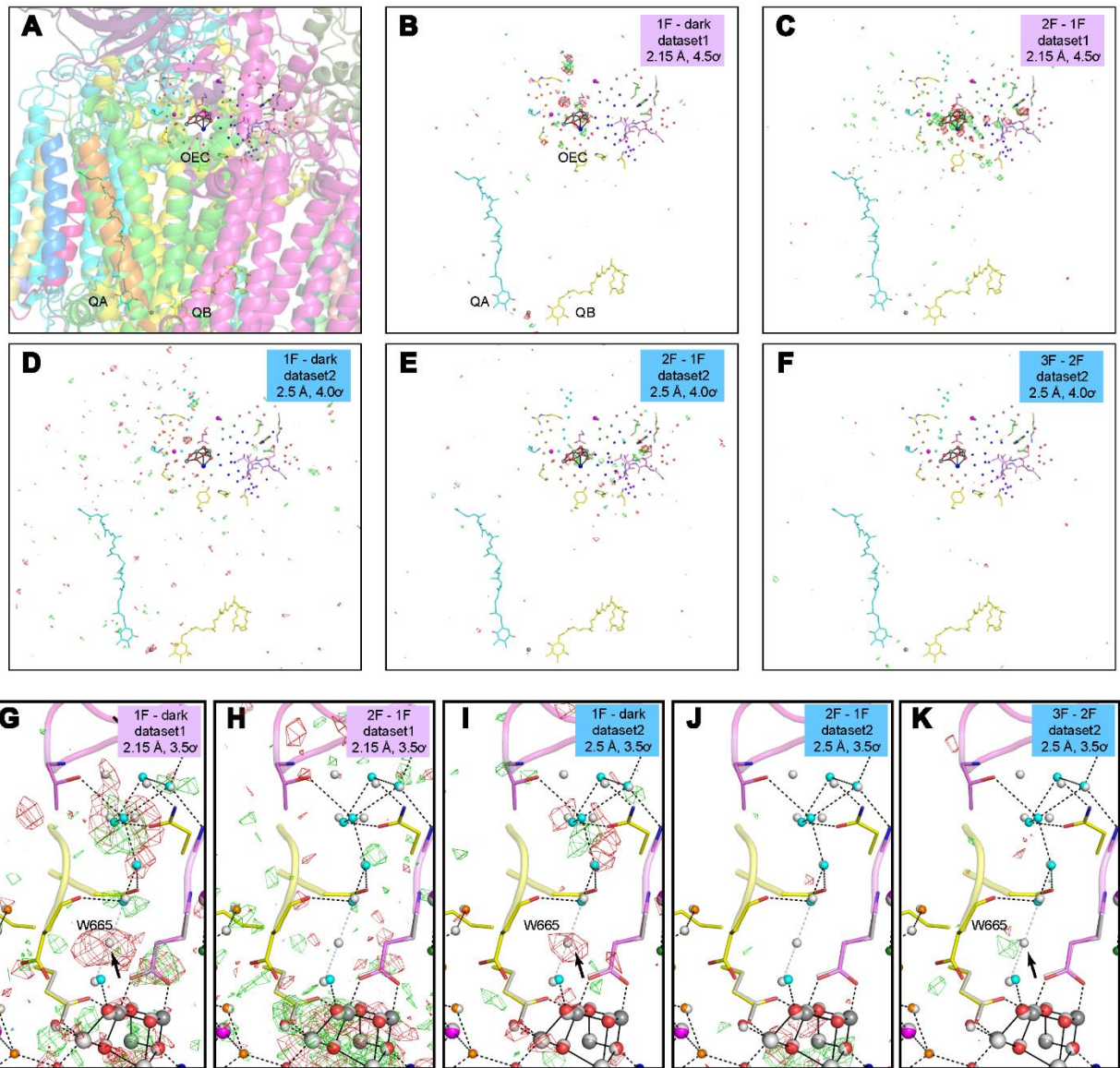


Fig. S3. Isomorphous difference Fourier maps between different S-states. **A.** Overall area of a PSII monomer, with the areas of OEC, O_A and Q_B-binding sites highlighted. **B, G,** $F_{\text{obs}} - F_{\text{obs}}$ difference map between datasets of 1F minus dark from dataset1. **C, H,** $F_{\text{obs}} - F_{\text{obs}}$ difference map between 2F minus 1F from dataset1. **D, I,** $F_{\text{obs}} - F_{\text{obs}}$ difference map between 1F minus dark from dataset2. **E, J,** $F_{\text{obs}} - F_{\text{obs}}$ difference map between 2F minus 1F from dataset2. **F, K,** $F_{\text{obs}} - F_{\text{obs}}$ difference map between 3F minus 2F from dataset2. View directions of (B-F) are the same as that of panel A. **G-K,** Enlarged view of the O4-channel. Boxes in (B-K) indicate the resolutions and contoured level of the maps. Structural changes found in W665 are indicated as arrows in (G, I, K).

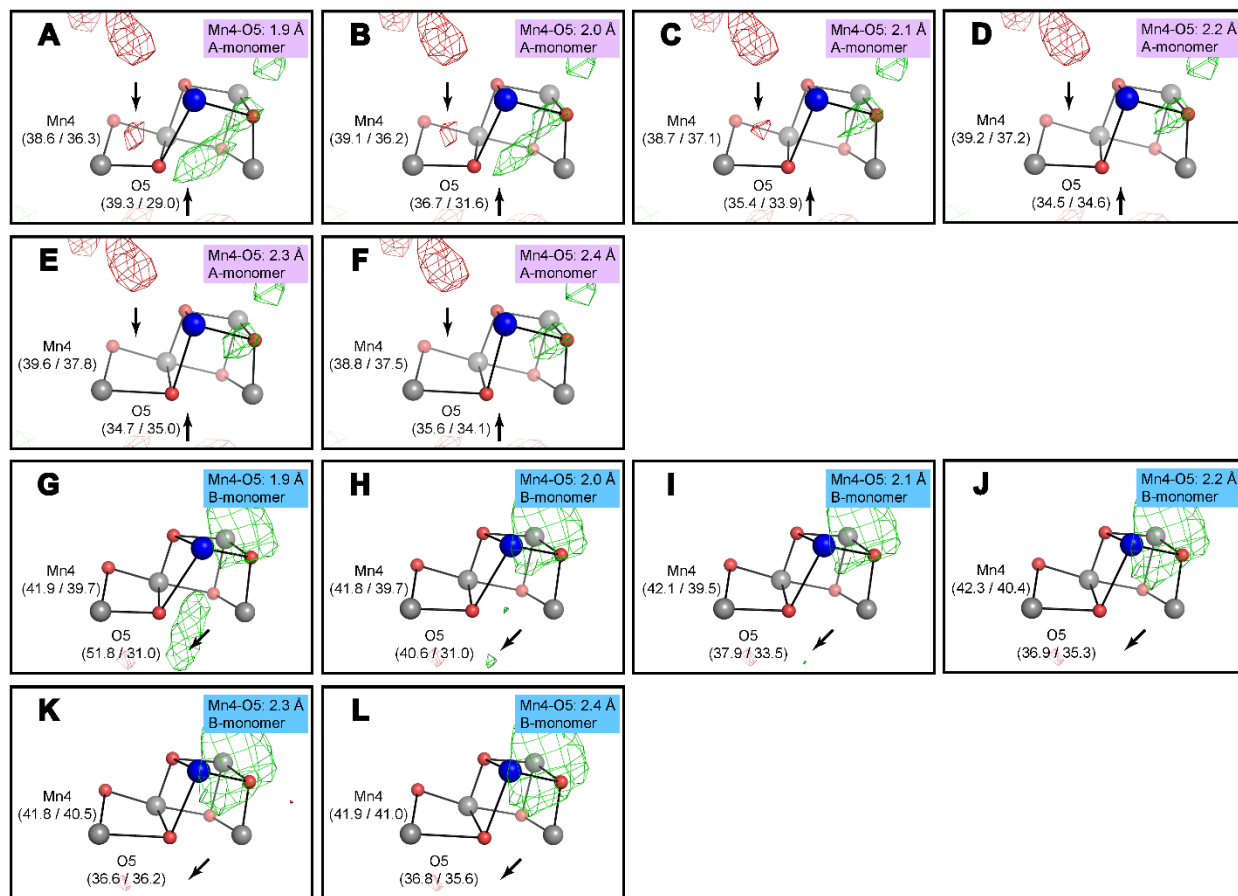


Fig. S4. mF_o-DF_c difference electron densities of the S_2 state structures refined under the different constraints for bond lengths between Mn4 and O5. mF_o-DF_c difference *Fourier* maps were contoured at -2.6σ (red) and $+2.2\sigma$ (green) with the structure refined with the constraints for bond distances of 1.9 Å (**A**, **G**), 2.0 Å (**B**, **H**), 2.1 Å (**C**, **I**), 2.2 Å (**D**, **J**), 2.3 Å (**E**, **K**), 2.4 Å (**F**, **L**), respectively. The difference electron densities were drawn around the OEC of the A-monomer (**A-F**) and B-monomer (**G-L**). The values in bracket indicate temperature factors of the structure with occupancies of 0.6 (left, refined the coordinate position) and 0.4 (right, fixed the coordinate position), respectively.

Table S1. Crystallographic data processing and refinement statistics.

PDB ID	dark-dataset1	1F-dataset1	2F-dataset1	dark-dataset2	1F-dataset2	2F-dataset2	3F-dataset2
	6JLJ	6JLK	6JLL	6JLM	6JLN	6JLO	6JLP
Data collection							
No. of collected images	123,200	120,000	123,200	217,566	100,400	155,520	181,440
No. of hit images	46,985	53,333	46,948	22,918	16,107	21,743	22,465
No. of indexed images	38,328	44,377	38,626	21,043	14,848	19,912	19,864
No. of images used for refinement	26,678	25,036	26,779	14,928	12,250	17,931	14,882
Space group	<i>P</i> 2 ₁ 2 ₁ 2 ₁			<i>P</i> 2 ₁ 2 ₁ 2 ₁			
Unit cell / Å	a = 122.0, b = 228.7, c = 287.0			a = 122.0, b = 228.8, c = 287.0			
Resolution / Å	50.0 - 2.15 (2.23 - 2.15)*	50.0 - 2.15 (2.23 - 2.15)*	50.0 - 2.15 (2.23 - 2.15)*	50.0 - 2.35 (2.44 - 2.35)*	50.0 - 2.40 (2.49 - 2.40)*	50.0 - 2.40 (2.49 - 2.40)*	50.0 - 2.50 (2.60 - 2.50)*
No. of unique reflections	407,701 (46,395)*	407,701 (46,395)*	407,701 (46,395)*	349,978 (34,692)*	328,402 (32,568)*	328,402 (32,568)*	290,301 (28,785)*
Completeness / %	100 (100)*	100 (100)*	100 (100)*	100 (100)*	100 (100)*	100 (100)*	100 (100)*
Multiplicity	1341 (734)*	1269 (695)*	1337 (735)*	781 (477)*	654 (445)*	955 (648)*	899 (611)*
$R_{\text{split}}^{\dagger}$	0.055 (0.656)*	0.054 (0.637)*	0.060 (0.715)*	0.078 (1.189)*	0.078 (1.209)*	0.070 (0.946)*	0.078 (0.910)*
CC _{1/2}	0.996 (0.287)*	0.996 (0.380)*	0.997 (0.231)*	0.995 (0.276)*	0.996 (0.273)*	0.997 (0.321)*	0.976 (0.372)*
mean I/σ (I)	10.6 (2.1)*	10.8 (2.2)*	11.0 (2.0)*	8.8 (1.2)*	8.3 (1.1)*	9.6 (1.4)*	9.4 (1.5)*
Refinement							
Resolution / Å	20.0 - 2.15	20.0 - 2.15	20.0 - 2.15	20.0 - 2.35	20.0 - 2.40	20.0 - 2.40	20.0 - 2.50
R factor / R _{free}	0.152 / 0.198	0.149 / 0.193	0.155 / 0.202	0.163 / 0.209	0.154 / 0.212	0.151 / 0.207	0.148 / 0.208
No. of reflections	407,701	407,701	407,701	349,978	328,402	328,402	290,301
Wilson B / Å ²	38.8	38.8	37.9	47.8	49.4	48.3	51.5
Average B (overall) / Å ²	55.5	54.9	53.4	60.3	66.5	66.1	68.0
Average B (protein) / Å ²	53.7	53.2	51.7	58.7	65.0	64.6	66.5
Average B (OEC) / Å ²	43.2	38.5	37.6	51.3	54.0	53.1	57.9
Average B (solvent) / Å ²	56.4	55.9	54.3	59.4	65.9	65.8	67.5
RMSD bond length / Å	0.008	0.010	0.009	0.008	0.010	0.010	0.010
RMSD bond angle / deg.	1.39	1.37	1.39	1.40	1.38	1.40	1.41
Ramachandran plot**							
Favored / Allowed / Outliers / %	97.8 / 2.1 / 0.1	97.8 / 2.1 / 0.1	97.7 / 2.1 / 0.2	97.5 / 2.3 / 0.2	97.2 / 2.6 / 0.2	97.2 / 2.6 / 0.2	96.8 / 3.0 / 0.2

*Values in parenthesis indicate those for the highest resolution shells.

$\dagger R_{\text{split}} = \sqrt{2 \sum |I_{\text{even}} - I_{\text{odd}}| / \sum (I_{\text{even}} + I_{\text{odd}})}$

**Calculated with MolProbability

Table S2. Statistics for the processing of the diffraction data for the dark-dataset1 (A), 1F-dataset1 (B), 2F-dataset1 (C), dark-dataset2 (D), 1F-dataset2 (E), 2F-dataset2 (F) and 3F-dataset2 (G)

A

resolution (Å)	observed unique reflections	completeness (%)	measured reflections	multiplicity	I/σ(I)	CC _{1/2}	R _{split} (%)
8.95	48,148	100	129,954,088	2,699	29.8	0.995	3.55
4.02	47,037	100	78,931,741	1,678	23.5	0.997	4.08
3.36	46,857	100	67,429,343	1,439	16.1	0.995	6.22
3.00	46,721	100	61,030,585	1,306	10.7	0.988	10.48
2.76	46,583	100	56,733,978	1,218	7.5	0.969	16.44
2.58	46,577	100	53,693,262	1,153	5.5	0.926	23.62
2.44	46,520	100	51,278,355	1,102	4.1	0.829	31.99
2.32	46,446	100	49,328,364	1,062	3.3	0.688	41.62
2.23	46,417	100	44,895,234	967	2.6	0.497	51.09
2.15	46,395	100	34,073,616	734	2.1	0.287	68.56
overall	467,701	100	627,348,566	1341	10.6	0.996	5.52

D

resolution (Å)	observed unique reflections	completeness (%)	measured reflections	multiplicity	I/σ(I)	CC _{1/2}	R _{split} (%)
9.79	36,123	100	53,107,121	1,470	25.4	0.994	4.30
4.40	35,236	100	31,141,358	884	21.6	0.995	4.66
3.68	35,070	100	26,078,364	744	14.3	0.974	7.77
3.29	34,933	100	23,200,949	664	8.8	0.975	13.62
3.02	34,862	100	21,298,325	611	5.6	0.936	23.27
2.82	34,835	100	19,889,086	571	3.8	0.856	35.99
2.67	34,734	100	18,790,199	541	2.7	0.663	51.37
2.54	34,766	100	17,948,469	516	2.0	0.578	70.38
2.44	34,727	100	17,193,072	495	1.5	0.388	95.40
2.35	34,692	100	16,539,820	477	1.2	0.276	118.88
overall	349,978	100	245,186,763	781	8.8	0.995	7.78

B

resolution (Å)	observed unique reflections	completeness (%)	measured reflections	multiplicity	I/σ(I)	CC _{1/2}	R _{split} (%)
8.95	48,148	100.0	123,098,267	2,557	28.3	0.994	3.66
4.02	47,037	100.0	74,718,024	1,589	23.5	0.997	4.04
3.36	46,857	100.0	63,806,890	1,362	16.7	0.995	5.85
3.00	46,721	100.0	57,707,545	1,235	11.5	0.989	9.35
2.76	46,583	100.0	53,609,920	1,151	8.2	0.975	14.49
2.58	46,577	100.0	50,712,973	1,089	6.0	0.943	21.12
2.44	46,520	100.0	48,406,512	1,041	4.5	0.867	29.02
2.32	46,446	100.0	46,541,484	1,002	3.6	0.770	36.92
2.23	46,417	100.0	42,469,314	915	2.9	0.590	46.02
2.15	46,395	100.0	32,258,942	695	2.2	0.380	63.65
overall	467,701	100.0	593,329,871	1269	10.8	0.996	5.40

E

resolution (Å)	observed unique reflections	completeness (%)	measured reflections	multiplicity	I/σ(I)	CC _{1/2}	R _{split} (%)
10.00	33,871	100	46,574,610	1,375	24.2	0.996	4.17
4.50	33,136	100	27,362,186	826	20.5	0.996	4.63
3.76	32,879	100	22,828,926	694	13.6	0.988	7.71
3.36	32,805	100	20,339,839	620	8.4	0.974	13.55
3.08	32,695	100	18,647,114	570	5.2	0.935	23.56
2.88	32,703	100	17,441,670	533	3.6	0.877	35.78
2.73	32,571	100	16,452,163	505	2.5	0.454	53.28
2.60	32,591	100	15,697,337	482	1.9	0.608	71.85
2.49	32,583	100	15,040,438	462	1.4	0.434	93.98
2.40	32,568	100	14,480,953	445	1.1	0.273	120.89
overall	328,402	100	214,865,236	654	8.3	0.996	7.82

C

resolution (Å)	observed unique reflections	completeness (%)	measured reflections	multiplicity	I/σ(I)	CC _{1/2}	R _{split} (%)
8.95	48,148	100.0	129,440,502	2,688	29.1	0.997	3.66
4.02	47,037	100.0	78,606,344	1,671	22.3	0.996	4.38
3.36	46,857	100.0	67,180,599	1,434	14.9	0.994	6.95
3.00	46,721	100.0	60,827,020	1,302	9.8	0.984	11.73
2.76	46,583	100.0	56,550,480	1,214	6.9	0.957	18.33
2.58	46,577	100.0	53,525,726	1,149	5.0	0.903	26.08
2.44	46,520	100.0	51,139,901	1,099	3.8	0.786	34.70
2.32	46,446	100.0	49,218,059	1,060	3.1	0.599	44.67
2.23	46,417	100.0	44,878,478	967	2.5	0.420	53.76
2.15	46,395	100.0	34,086,304	735	2.0	0.231	71.50
overall	467,701	100.0	625,453,413	1337	11.0	0.997	5.98

F

resolution (Å)	observed unique reflections	completeness (%)	measured reflections	multiplicity	I/σ(I)	CC _{1/2}	R _{split} (%)
10.00	33,871	100	68,098,729	2,011	27.4	0.996	3.77
4.50	33,136	100	39,998,548	1,207	23.7	0.997	4.09
3.76	32,879	100	33,346,754	1,014	15.5	0.985	7.08
3.36	32,805	100	29,698,139	905	9.6	0.972	12.07
3.08	32,695	100	27,199,162	832	6.0	0.948	20.36
2.88	32,703	100	25,444,064	778	4.2	0.881	30.18
2.73	32,571	100	24,002,837	737	3.0	0.657	44.06
2.60	32,591	100	22,905,887	703	2.2	0.570	59.39
2.49	32,583	100	21,941,127	673	1.7	0.484	75.40
2.40	32,568	100	21,111,639	648	1.4	0.321	94.63
overall	328,402	100	313,746,886	955	9.6	0.997	6.99

G

resolution (Å)	observed unique reflections	completeness (%)	measured reflections	multiplicity	I/σ(I)	CC _{1/2}	R _{split} (%)
10.41	30,001	100	56,624,647	1,887	24.6	0.993	4.43
4.69	29,273	100	33,235,143	1,135	22.1	0.995	4.66
3.92	29,074	100	27,743,710	954	16.1	0.987	6.92
3.50	29,001	100	24,707,349	852	10.3	0.313	13.57
3.21	28,929	100	22,668,324	784	6.7	0.949	19.12
3.01	28,825	100	21,122,876	733	4.6	0.894	28.97
2.84	28,848	100	20,016,447	694	3.3	0.804	41.60
2.71	28,798	100	19,040,620	661	2.5	0.615	56.90
2.60	28,767	100	18,251,934	635	1.9	0.485	73.79
2.50	28,785	100	17,595,793	611	1.5	0.372	90.98
overall	290,301	100	261,006,843	899	9.4	0.976	7.84

Table S3. R_{iso} values between the datasets of dataset1 (A), dataset2 (B) and those reported by Kern et al. (C) (16).

A

	1F-dataset1	2F-dataset1
dark-dataset1	0.073 (0.211)*	0.078 (0.227)*
1F-dataset1	-	0.081 (0.269)*
2F-dataset1		-

B

	1F-dataset2	2F-dataset2	3F-dataset-2
dark-dataset2	0.116 (0.263)*	0.127 (0.263)*	0.116 (0.269)*
1F-dataset2	-	0.096 (0.233)*	0.099 (0.234)*
2F-dataset2		-	0.096 (0.236)*

C

	1F (6DHF)	2F (6DHO)	3F (6DHP)
dark (6DHE)	0.123 (0.284)*	0.119 (0.264)*	0.116 (0.262)*
1F (6DHF)	-	0.126 (0.264)*	0.121 (0.265)*
2F (6DHO)		-	0.119 (0.264)*

*Values in parenthesis indicate those for the highest resolution shells.

Table S4. Interatomic distances of the OEC in different S-states.

	Color code*	dark-dataset1			6DHE	1F-dataset1			6DHF	2F-dataset1			6DHP
		A	B	Average	Kern et. al.	A	B	Average	Kern et. al.	A	B	Average	Kern et. al.
Mn1-Mn2	+0.1 <	2.58	2.61	2.60	2.78	2.69	2.67	2.68	2.81	2.57	2.59	2.58	2.75
Mn1-Mn3	+0.05 to +0.1	3.19	3.13	3.16	3.25	3.24	3.17	3.21	3.26	3.31	3.30	3.31	3.33
Mn1-Mn4	+0.03 to +0.05	4.98	4.95	4.97	4.86	4.92	4.87	4.90	4.86	5.28	5.14	5.21	5.06
Mn2-Mn3	0 to +0.03	2.71	2.72	2.72	2.85	2.76	2.73	2.75	2.84	2.72	2.70	2.71	2.86
Mn2-Mn4	-0.03 to 0	5.29	5.24	5.27	5.21	5.22	5.17	5.20	5.24	5.36	5.26	5.31	5.25
Mn3-Mn4	-0.05 to -0.03	2.92	2.86	2.89	2.74	2.75	2.76	2.76	2.74	2.91	2.89	2.90	2.77
Mn1-Ca	-0.1 to -0.05	3.59	3.63	3.61	3.43	3.50	3.52	3.51	3.42	3.50	3.50	3.50	3.37
Mn2-Ca	< -0.1	3.42	3.42	3.42	3.38	3.40	3.39	3.40	3.41	3.47	3.45	3.46	3.33
Mn3-Ca		3.33	3.46	3.40	3.51	3.42	3.50	3.46	3.52	3.42	3.57	3.50	3.57
Mn4-Ca		3.69	3.82	3.76	3.83	3.88	3.91	3.90	3.90	3.97	3.98	3.98	4.01
Mn1-O5		2.70	2.69	2.70	2.70	2.79	2.72	2.76	2.74				
Mn3-O5		2.03	2.03	2.03	2.10	2.07	1.99	2.03	2.06	1.90	1.90	1.90	2.00
Mn4-O5		2.31	2.31	2.31	2.13	2.20	2.20	2.20	2.18	2.20	2.20	2.20	2.22
Mn1-O6										1.70	1.71	1.71	1.80
O5-O6										1.90	1.89	1.90	2.09

*Color codes were shown for distances with changes in the designated ranges during the S-state transitions. Numbers without colors indicate no apparent changes.

Table S5. Comparison of interatomic distances within OEC in the S₃ state obtained in the present study with those geometrically optimized by QM/MM methods (31).

	2F-dataset1	Hydroxo /oxo	Hydroxo /oxo	Oxo/oxo	Oxyl/oxo	Oxo/oxo	peroxo	superoxo
Cubane	Open	Open	Close	Open	Open	Close	Open	Open
Mn ₄ -Mn ₃	2.90	2.78	3.26	2.75	2.86	3.06	2.91	3.05
Mn ₃ -Mn ₂	2.71	2.82	2.76	2.80	2.78	2.74	2.75	2.78
Mn ₂ -Mn ₁	2.58	2.76	2.70	2.77	2.75	2.74	2.76	2.74
Mn ₃ -Mn ₁	3.31	3.55	2.88	3.31	3.34	3.02	3.30	3.37
Mn ₄ -Mn ₁	5.21	5.22	5.29	5.18	5.19	5.13	5.11	5.09
Mn ₄ -O ₅	2.20	1.81	1.77	1.79	2.16	1.67	2.27	2.24
Mn ₁ -O ₅	1.71	1.77	1.82	1.66	1.68	2.14	2.17	2.33
O ₅ -O ₆	1.90	2.42	2.64	2.28	1.94	1.99	1.42	1.33

Table S6. Nomenclature for water molecules

Water 4UB6	dark-dataset1 6JLJ	1F-dataset1 6JLK	2F-dataset1 6JLL	Kern et. al. (16) 6DHF
W567	523	525	520	W19
W665	699 (C)	683 (C)	NA	W20
W542	566	569	570	W48
W546	562	582	574	W49
W612	820 (C)	817 (C)	795 (C)	W50
W806	657 (C)	675 (C)	656 (C)	W52
W548	586	559	557	W53
W606	528	544	551	W51
W757	603 (C)	602 (C)	NA	NA
W571	651	655	NA	622 (A)
W503	650	657	653	W32
W547	595	613	616	W27
W554	543	558	549	W30
W666*	NA	NA	NA*	NA
W667*	NA	NA	NA*	NA

* These waters were not built in the coordinate.